DPW-7: Steady and Unsteady Computations of the Common Research Model at Different Reynolds Numbers

David Hue, Fulvio Sartor, Ilias Petropoulos, Camille Fournis

DPW-7: Steady and Unsteady Computations of the CRM Aircraft at Different Reynolds Numbers

David Hue[1], Fulvio Sartor[2], Ilias Petropoulos[3], Camille Fournis[4]
ONERA, The French Aerospace Lab, 92190 Meudon, France

This article presents the numerical computations performed at ONERA for the 7th AIAA Drag Prediction Workshop. By introducing Reynolds numbers up to 30 million closer to the flight conditions, greater lift levels beyond the design point, and time-accurate simulations, this new session has allowed the previous studies to be extended. The CRM aircraft configuration has been considered in its academic Wing-Body version and calculated in this work with the point-matched structured grids provided by J. Vassberg. The ONERA Cassiopee software, as well as the elsA solver and the FFDπ far-field drag code have been used. The grid convergence study has shown larger pressure drag variations than what was obtained at cruise lift coefficient, but increasing the Reynolds number seems to reduce this trend. Then, the Angle-of-Attack sweep study with the lift, drag, and moment polars has been the opportunity to assess different numerical settings such as the SA and kω-SST turbulence models with the QCR-2000 approach, and to discuss the comparison between CFD results and wind tunnel data. Concerning the Reynolds number increase, it has appeared that the main part of drag reduction comes from the friction (~60%) and viscous pressure drag (~30%) components. The prediction of pitching moment increments, in this case due to Reynolds number variations, is still to be significantly improved. Finally, for *AoA* above 4.00°, by the use of URANS computations, an unsteady buffet phenomenon has been observed and analysed.

[1] Engineer, Applied Aerodynamics Department, david.hue@onera.fr, DPW Committee Member.
[2] PhD, Applied Aerodynamics Department, fulvio.sartor@onera.fr, Senior Research Engineer.
[3] PhD, Applied Aerodynamics Department, ilias.petropoulos@onera.fr, Research Scientist.
[4] PhD, Applied Aerodynamics Department, camille.fournis@onera.fr, Research Scientist.

Nomenclature

AoA	=	angle of attack
AR	=	aspect ratio
b	=	wing span
c	=	wing chord
CDf	=	friction drag coefficient
CDff	=	far-field drag coefficient
CDi	=	lift-induced drag coefficient
CDnf	=	near-field drag coefficient
CDp	=	pressure drag coefficient
CDsp	=	spurious drag coefficient
CDv	=	viscous drag coefficient
CDvp	=	viscous pressure drag coefficient
CDw	=	wave drag coefficient
Cf	=	skin friction coefficient
CL	=	lift coefficient
CM	=	pitching moment coefficient
Cp	=	pressure coefficient
h	=	grid factor
Ma	=	Mach number
Re	=	Reynolds number
Sref	=	reference surface area
u, v, w	=	x, y, z velocity components
Y^+	=	normalized first cell height
η	=	fraction of wing span
∞	=	subscript for freestream state value

I. Introduction

STARTED in 2001, the Drag Prediction Workshop (DPW) [1,2] series is aimed at assessing the existing Computational Fluid Dynamics (CFD) methods used for civil aircraft aerodynamic performance prediction.

In 2022, the Aerodynamics, Aeroelasticiy, and Acoustics Department (DAAA) of ONERA took part in the 7th edition of DPW as it did in DPW-2, DPW-4 [3], DPW-5 [4,5], and DPW-6 [6,7,8] . For this workshop, the geometry is once again the Common Research Model (CRM) [9,10] and only the Wing-Body (WB) configuration is considered. Indeed, while the previous workshop introduced a more complex geometry with the Nacelle-Pylon installation, this one is aimed at "Expanding the envelope": greater Reynolds numbers and higher Angles of Attack (*AoA*) are studied, unsteady computations are carried out. As in DPW-6, there are different wing geometries to ensure that the numerical shapes match the twist and bending values which were measured in wind tunnels for *AoA* from 2.50 to 4.25 degrees.

The paper is classically organized as follows: first, the CRM geometry mentioned above and the structured grids that have been used for these computations will be described. The Navier-Stokes (NS) solver and the far-field drag analysis code involved in this work will be introduced. Afterwards, the results including grid convergence at a larger lift level than previously, *AoA* sweep studies, Reynolds number effects from 5 to 30 million will be shown. Finally, a section will be dedicated to the Unsteady Reynolds-Averaged-Navier-Stokes (URANS) calculations performed at the highest *AoA* to investigate the transonic buffet phenomenon.

II. CRM Geometries and Grids

A. CRM Wing Geometries

As mentioned in the introduction, even if only the Wing-Body configuration is used in DPW-7, there are several CRM geometries to consider. Indeed, the deformation is taken into account according to the *AoA* and so the associated wing loading: twist and bending values evolve along the polar. The European Transonic Wind tunnel (ETW) measurements have been chosen as a reference [7,11] and in the end, there are eight different wing geometries for the following *AoA*: 2.50, 2.75, 3.00, 3.25, 3.50, 3.75, 4.00, and 4.25 degrees.

As a reminder for this now famous geometry since DPW-4 in 2009, the CRM was designed by an AIAA Technical Working Group [9] and it exhibits standard characteristics: conventional low wing configuration, design Mach number of 0.85, fuselage representative of a wide body commercial aircraft. The WB configuration is shown in Fig. 1.

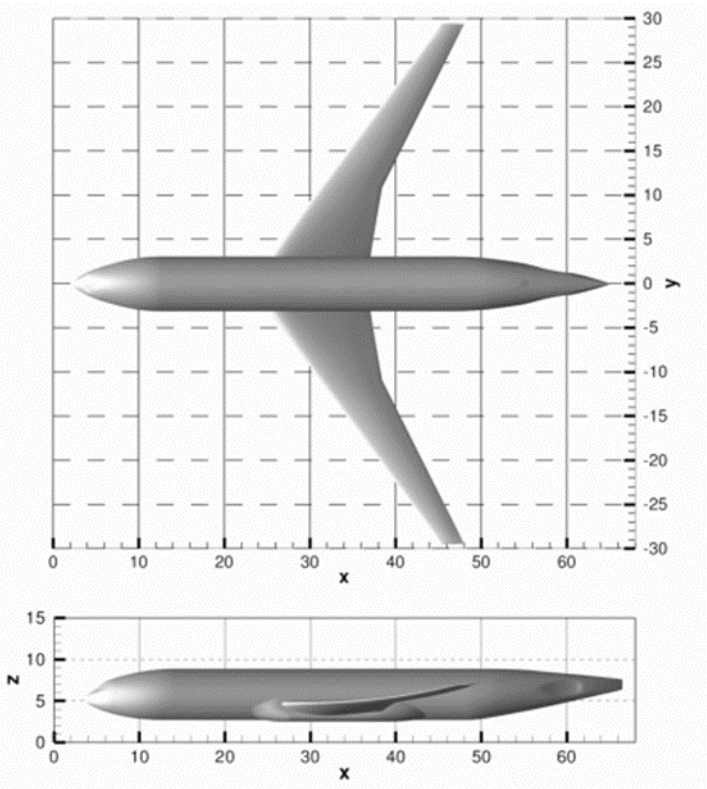

Fig. 1 CRM wing-body configuration.

This geometry is defined by a mean-aerodynamic chord c = 7.00532 m, a reference surface area *Sref* = 383.6896 m^2 (full-model), a semispan $b/2$ = 29.38145 m, an aspect ratio *AR* = 9.0, and a moment center *Xref* = 33.6776 m, *Yref* = 0.0 m, and *Zref* = 4.5203 m.

Fig. 2. shows the difference between the initial DPW-5 wing geometry and some of the ones based on experiments and used in DPW-6 and DPW-7. The bending is significantly different but this parameter is known to have a limited impact on the drag polar [12]. However, the twist variation, which was studied in [5], even if it is less visible, does imply non-negligible effects. With the highest *AoA*, the loading produces more pronounced nose-down profile sections in the outboard wing.

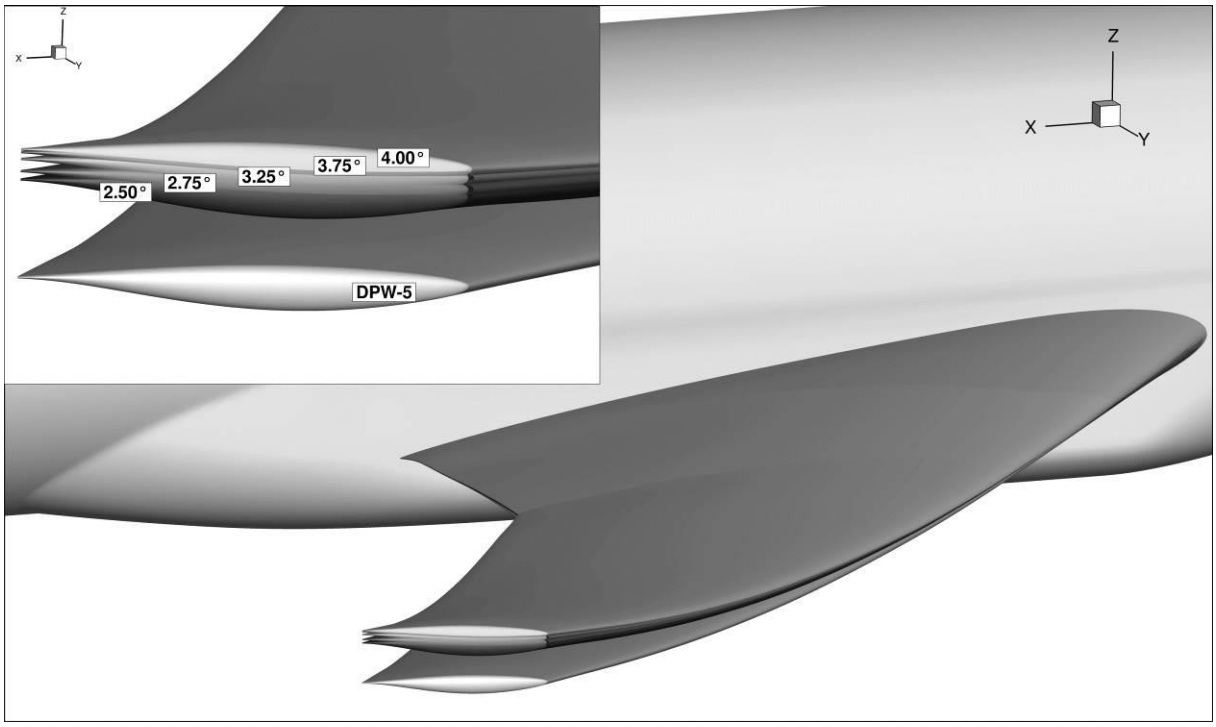

Fig. 2 CRM wing shapes at different angles of attack.

B. Structured Multiblock Grids

To run the computations of this study, the multiblock point-matched grids kindly provided by John Vassberg have been used (Vassberg_Grids.REV00 [13]). They are similar to the ones for DPW-5 presented in [14].

The point-matched grid family is composed of 6 grids exhibiting different refinement levels from Tiny to Ultra Fine corresponding to the 3.00° geometry, 7 other grids of Medium refinement corresponding respectively to 2.50°, 2.75°, 3.25°, 3.50°, 3.75°, 4.00°, and 4.25° wing geometries in low dynamic pressure conditions (LoQ), plus an additional Medium grid of a 2.50° geometry in high dynamic pressure conditions (HiQ). These 14 grids have been generated for a Reynolds number of 30 million but the DPW Committee decided they could be used for all the workshop computations with Reynolds numbers varying from 5 to 30 million. This implies that the normalized first cell height Y^+ can be very small ($Y^+ < 0.1$) for the Medium to finest grids calculated at Re = 5 million. A posteriori, it led to no issue, the friction drag prediction in particular was not affected.

Table 1 presents the 6 grids that are used for the convergence study, the other grids have the Medium characteristics. They range from 5.3 to 221.3 million points, corresponding for this grid family to a size ratio of about 42, which is intermediate between the DPW-6 (Overset grids) and DPW-5 values in ONERA studies, i.e. respectively 8 and 200. All the grids are built on a semi-configuration with an O-type topology composed of 5 structured blocks (i, j, k), as illustrated in Fig. 3 showing a plane Index(i) = constant on the suction side as well as the symmetry plane. They have at least 2 constantly-spaced cells at viscous walls (2 for Tiny, 4 for Medium, 7 for Ultra Fine). The growth rates do not exceed 1.2, the wing spanwise spacing is below 0.1% of semispan at root and tip, and the chordwise spacing is under 0.1% of local chord length at leading and trailing edges, the trailing edge itself being discretized by at least 8 cells. The farfield boundary is located at more than 100 semispan lengths.

It is interesting to notice that the Medium grid refinement of DPW-7 corresponds to the one of the Extra Fine grid of DPW-5 [14], showing the substantial grid size evolution over the past ten years. Fig. 4 gives the different refinement levels on the symmetry plane, fuselage, and wing from Tiny grid to Medium and Extra Fine.

Table 1 Point-matched multiblock grids Vassberg_Grids.REV00

Level	Name	Number of points (N)	Y^+
L1	Tiny (T)	5,286,597	1.00
L2	Coarse (C)	17,644,325	0.67
L3	Medium (M)	41,590,149	0.50
L4	Fine (F)	80,957,925	0.40
L5	Extra Fine (X)	139,581,509	0.33
L6	Ultra Fine (U)	221,294,757	0.29

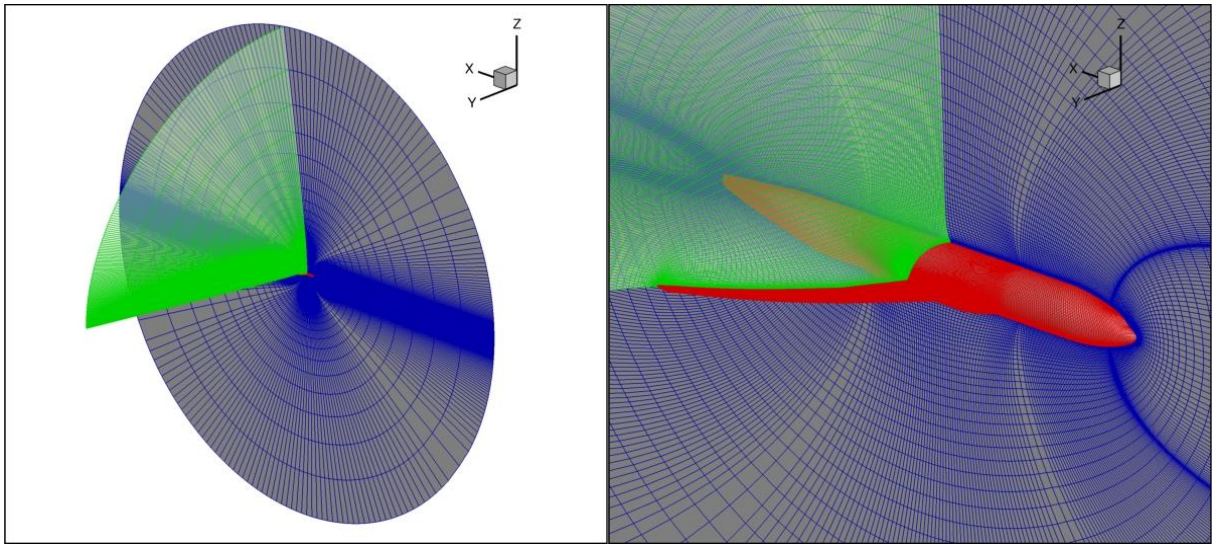

Fig. 3 Illustration of the Vassberg multiblock grid topology (Tiny).

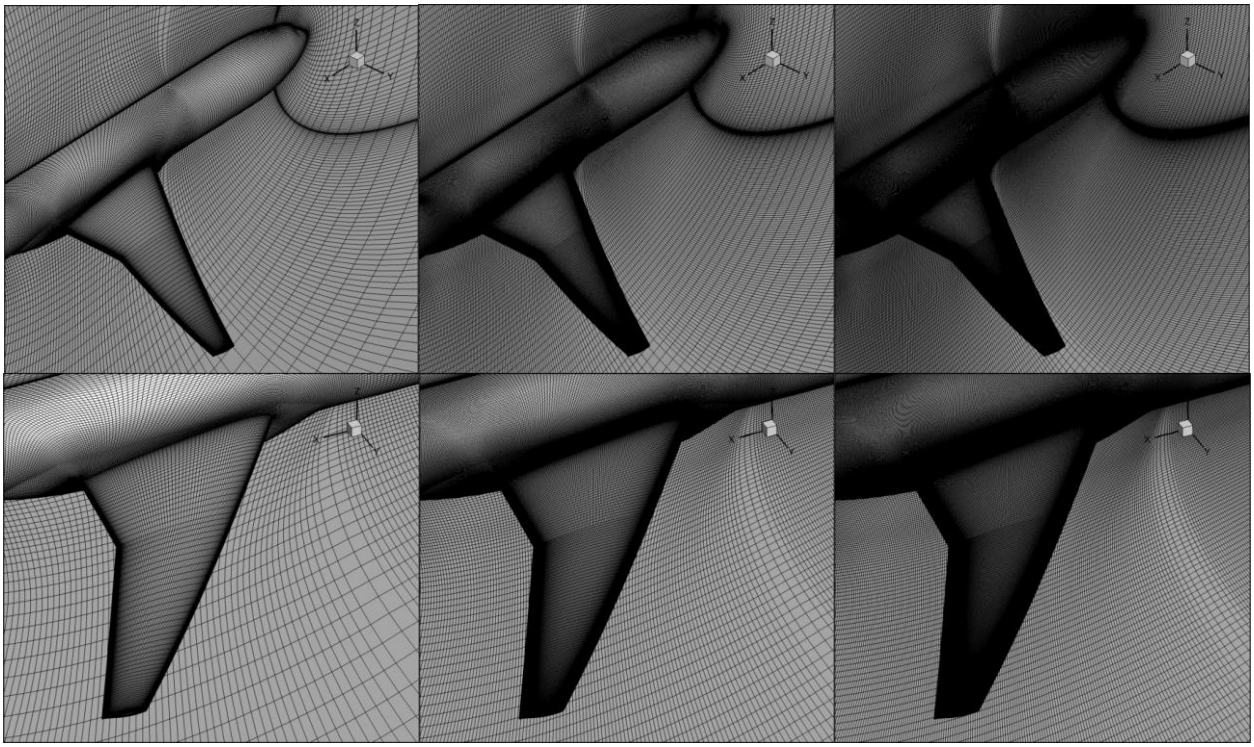

Fig. 4 Illustration of refinement levels: Tiny grid at left, Medium in the middle, and Extra Fine at right.

Concerning grid format, they were initially produced in the so-called plot3d data format. For the computations presented in this article it was necessary to convert them into CGNS files (CFD General Notation System) [15]. It

has been done with the ONERA tool Cassiopee [16]. The obtained CGNS files are now shared with the community and downloadable on the DPW-7 website [17]. They include the grid connectivities and boundary conditions.

III. Solver and Far-Field Post-Processing

C. elsA Solver

The RANS and URANS computations presented here are performed with the elsA solver [18]. This software uses a cell-centered finite-volume discretization on structured point-matched and Overset grids or unstructured grids. In this study, only the structured mode is used. For RANS, the time integration is carried out by a backward-Euler scheme with implicit LU-SSOR relaxation, for URANS Gear's formulation is applied with a time-step of 5 x 10^{-5} seconds (corresponding to roughly 1600 steps per period), with each step converged during 8 inner iterations. The spatial discretization is realized using a 2nd order centered scheme with Jameson-like artificial dissipation [19]. Multigrid techniques with one coarse grid level are generally used to accelerate convergence. All the computations are fully turbulent, potential laminar flow over the aircraft is not taken into account. Turbulence effects are simulated by the one-equation Spalart-Allmaras (SA) model [20] and for some specific calculations by the kω-SST model of Menter [21]. The Quadratic Constitutive Relation (QCR-2000) [22], a nonlinear closure which is not based on the traditional Boussinesq relation, has been employed.

In order to reach a satisfactory level of convergence, the computations were continued at least until the fluxes were stable enough to observe a lift coefficient variation lower than +/- 0.001 and a drag coefficient variation lower than 0.5 drag count over the last thousand iterations (1 drag count = 10^{-4}). For example, this is illustrated in Fig. 5 which exhibits the residual and force coefficient curves obtained over 20,000 iterations on the Medium refinement level in the grid convergence study. It is noticed that the friction drag component shows a much faster convergence than the pressure drag. The numerical behavior obtained with these multiblock grids was globally very good but convergence issues were encountered with the Ultra Fine grid. With the latter, no results could be obtained for a Reynolds number of 5 million and the multigrid acceleration had to be turned off to reach convergence at 20 million.

Concerning computotional aspects, the elsA simulations were executed on the ONERA internal cluster. The computations carried out for this work were performed in parallel mode, using from 28 to 1064 cores (from Tiny to Ultra Fine). A steady-state calculation on the Medium grid took approximately 10 hours on 196 cores and an unsteady one about 5 hours for each buffet period on 384 cores.

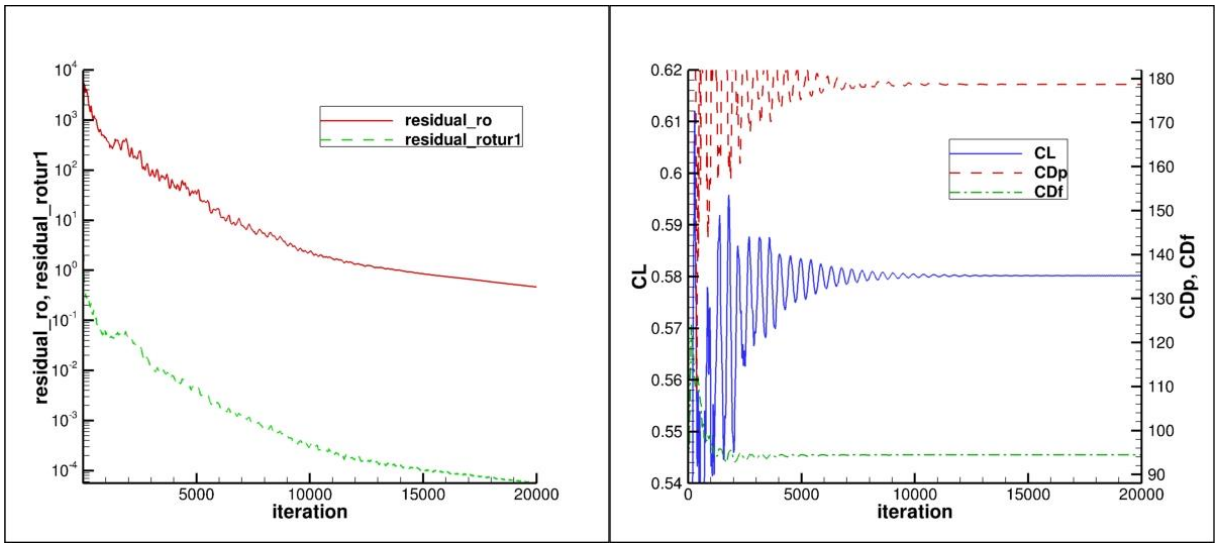

Fig. 5 WB; *Ma* = 0.85, *Re* = 20 x10^6, *CL* = 0.58; residual and force coefficient convergence, Medium grid.

D. Far-Field Drag Analysis

The standard and most straightforward method to compute aerodynamic performance coefficients consists in integrating forces on the aircraft skin, referred to as a near-field approach. On the other hand, far-field methods consist in evaluating the effect of the aircraft on the fluid through a momentum balance. Particular modeling considerations of this type then lead to a phenomenological decomposition of drag. The formulations and methods relative to the far-field theory have been presented in former ONERA publications [3,23,24,25]. In the present study, all the far-field analyses are carried out with the drag extraction code FFDπ [26], coupled with the Cassiopee library of ONERA [16].

The far-field drag analysis aims at providing a physical drag breakdown into viscous, wave, and lift-induced drag components. In addition, this analysis can isolate an important part of the spurious drag, related to numerical approximation errors (e.g. numerical dissipation and grid quality). In practice, this analysis is carried out at the end of the CFD process, as a post-processing tool working on the numerical solutions provided by the solver.

The different drag coefficients which are used in this article are defined below. Near-field drag is defined as the sum of pressure and friction drag:

$$CD_{nf} = CD_p + CD_f \quad \textbf{(1)}$$

Far-field drag is defined as the sum of the viscous, wave and induced drag components:

$$CD_{ff} = CD_v + CD_w + CD_i \quad \textbf{(2)}$$

$$CD_{sp} = CD_{nf} - CD_{ff} \quad \textbf{(3)}$$

The spurious drag *CDsp* is defined as drag generated through entropy or stagnation enthalpy variations along streamlines outside physical viscous layers and shocks, and not resulting from vortex decay [23]. It is generally produced in regions of strong pressure gradients via the addition of artificial dissipation. The viscous pressure drag *CDvp* is the part of the viscous drag which is not directly associated to the friction drag (displacement or wake effect, flow separation):

$$CD_v = CD_{vp} + CD_f \quad \textbf{(4)}$$

The far-field formulation allows for the following near-field/far-field drag balance:

$$CD_p + CD_f = CD_v + CD_w + CD_i + CD_{sp} \quad \textbf{(5)}$$

Fig. 6 shows a view of the integration volumes of the viscous pressure and wave drag components on the Medium grid at cruise lift coefficient and high-dynamic-pressure conditions. Such visualizations can highlight interesting modifications of the shock features, especially in design and optimization processes.

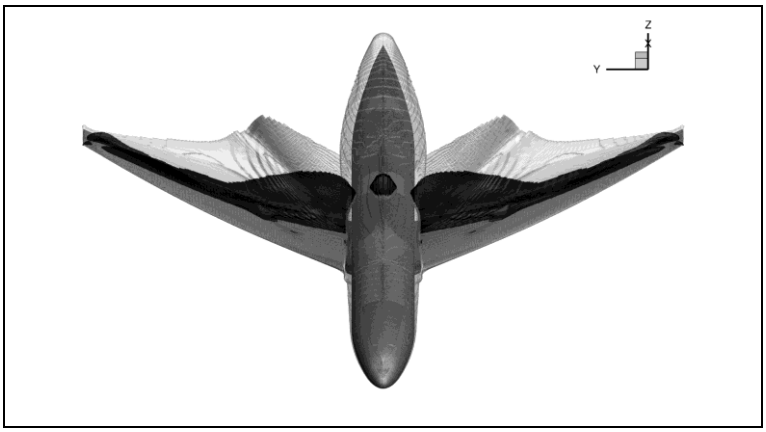

Fig. 6 WB; *Ma* = 0.85, *Re* = 30 x 10^6, *CL* = 0.5; integration volumes for *CDw* (black) and *CDvp* (grey).

IV. The Grid Convergence Study

In this section, the results of the grid convergence study proposed in DPW-7 are presented. Contrary to the previous workshops, the targeted lift coefficient *CL* is not 0.5. Indeed, a greater coefficient of 0.58 has been chosen, implying significantly different flow characteristics over the wing. Furthermore, the grid convergence study, formerly carried out with a Reynolds number limited to 5 million, is now extended to 20 million, which is more representative of flight conditions. All the drag coefficients are given in drag counts (d.c.).

A. Switching from *CL* = 0.5 to 0.58

Before discussing the results of the grid convergence, it is important to underline that DPW-4, DPW-5, and DPW-6 did use the aircraft design point for the lift coefficient of these studies. Here, the lift coefficient is stronger, at the gates of the non-linear zone in *CL*(*AoA*). A focus is given to compare the two different conditions. As the Reynolds number of previous editions was 5 million, the DPW-7 computations presented here are realized with the same value.

First, Table 2 shows the near-field and far-field global coefficients for three geometries, two of them at a lift level of 0.5 and the last one at 0.58. The columns DPW-6 and DPW-7 at *CL* = 0.5 correspond to SA QCR-2000 computations performed with different grid types, Overset and point-matched grids respectively, and slightly different wing geometries, A275 and A250. Nevertheless, they exhibit consistent results with a very good agreement between the DPW-6 and DPW-7 calculations at design point. The third column deals with the geometry corresponding to an *AoA* of 3.00° (A300) that is aimed at computations targeting *CL* = 0.58. Finally, the Delta

column demonstrates the significant difference existing between the cases *CL* = 0.5 and 0.58. The total drag is subjected to an increase of more than 20%, i.e. about 56 counts from 255 to 311. The wave drag is particularly impacted with a penalty of around 16 counts representing almost 30% of the total drag increase.

Table 2 WB; *Ma* = 0.85, *Re* = 5 x 10^6, *CL* = 0.5 and 0.58; global coefficients

	DPW-6 CL = 0.50	DPW-7 CL = 0.50	DPW-7 CL = 0.58	Delta (DPW-7)
Alpha (°)	2.469	2.425	3.000	0.575
CL	0.50	0.5	0.58	0.080
CM	-0.0922	-0.0957	-0.1054	-0.0097
CDnf	255.0	254.8	310.6	55.8
CDp	140.8	140.6	198.0	57.4
CDf	114.2	114.2	112.7	-1.5
CDvp	42.9	42.2	52.5	10.3
CDv	157.1	156.4	165.2	8.8
CDw	6.2	6.1	22.3	16.2
CDi	91.9	92.4	123.4	31.0

These substantial differences in flow can be observed in Fig. 7, where the pressure distributions at 50 and 95% of span show the much more important wing loading in the first part of the profile at *CL* = 0.58, as well as the impact on the shock position and intensity. This has to be kept in mind when comparing the convergence study of DPW-7 to the ones of previous workshops.

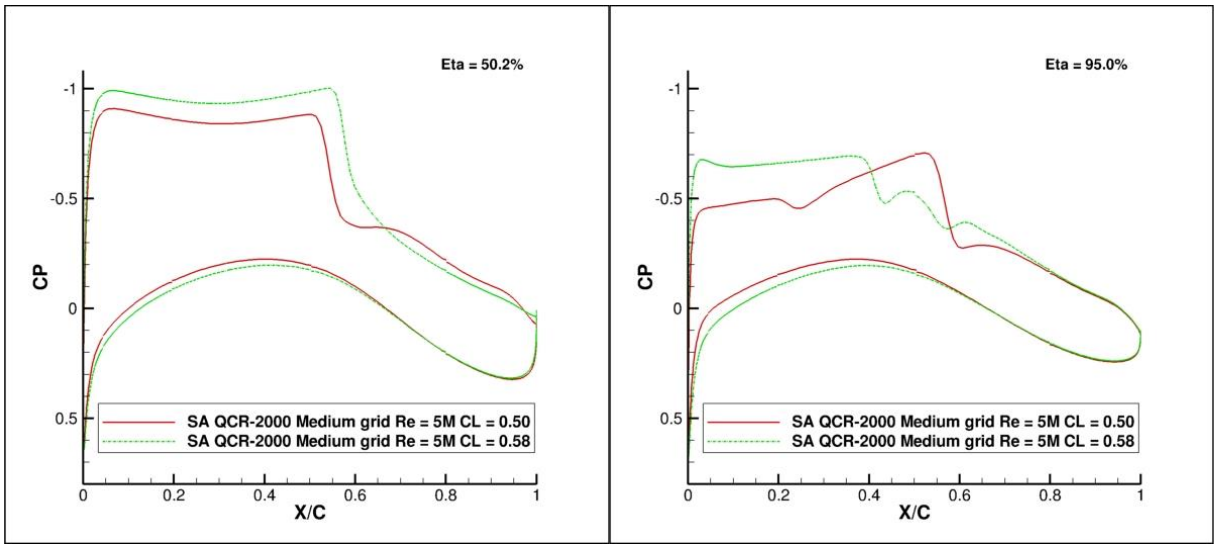

Fig. 7 WB; *Ma* = 0.85, *Re* = 5 x 10^6, *CL* = 0.5 and 0.58; wing pressure distributions.

B. DPW-7 Convergence Studies

For the grid convergence results presented below, the wing geometry is the one named A300 and the grids are the ones of Table 1. The aerodynamic conditions are the following: Mach number *Ma* = 0.85, Reynolds number of 5 and 20 million, and lift coefficient *CL* = 0.58 (±0.001).

In Fig. 8, the classical grid convergence curves are shown. The pressure and friction drag coefficients obtained with the different grids are given according to the refinement level (coarsest grids on the right, finest ones on the left). Some DPW-6 ONERA results [6] obtained with Overset grids and for *CL* = 0.5 are plotted for comparison. Then, Table 3 goes through the DPW-7 convergence with the Reynolds number of 20 million by showing all the near-field and far-field components. The far-field drag analysis was carried out for the first five grid levels.

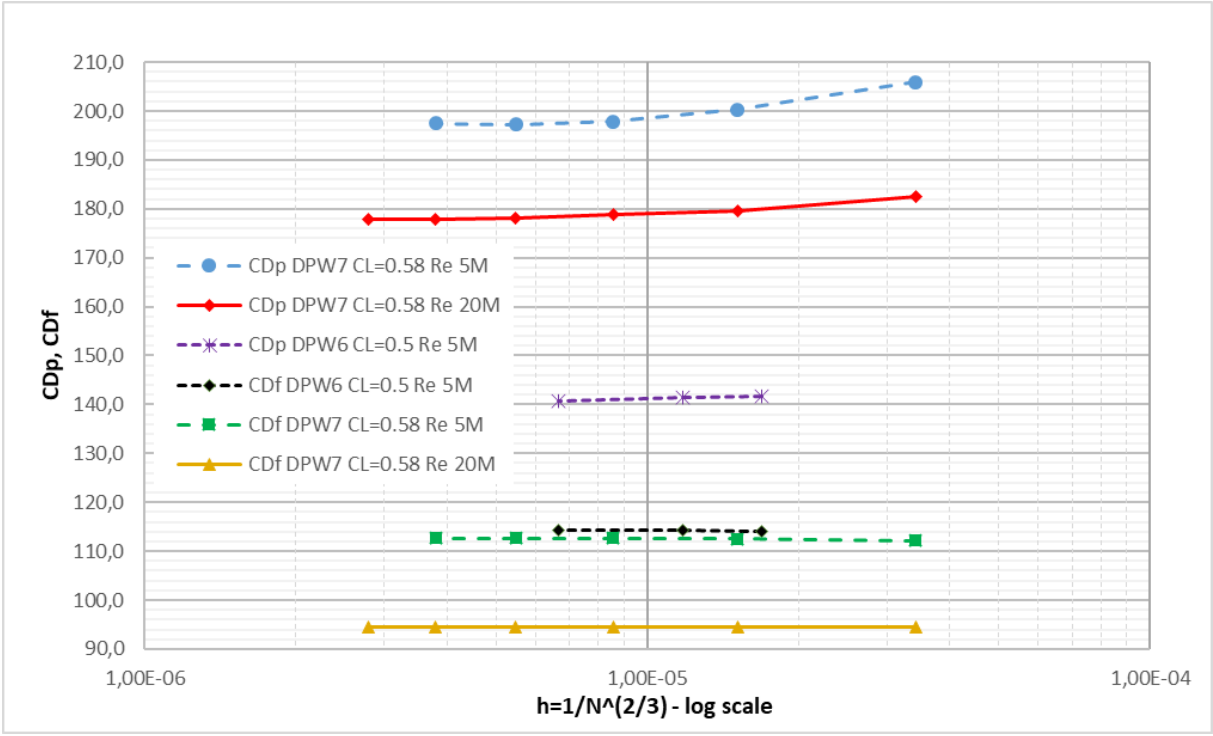

Fig. 8 WB; *Ma* = 0.85, *Re* = 5 and 20 x 10^6, *CL* = 0.5 and 0.58; grid convergence curves.

Table 3 WB; Ma = 0.85, Re = 20 x 10^6, CL = 0.58; global coefficients

Grid Level	L1	L2	L3	L4	L5	L6
Alpha (°)	2.785	2.760	2.755	2.750	2.750	2.750
CM	-0.1218	-0.1239	-0.1248	-0.1251	-0.1254	-0.1259
CDnf	277.1	273.9	273.2	272.6	272.6	272.3
CDp	182.7	179.5	178.8	178.1	178.1	177.9
CDf	94.4	94.4	94.4	94.5	94.5	94.4
CDvp	41.8	39.7	38.9	38.6	38.4	-
CDv	136.2	134.1	133.3	133.1	132.9	-
CDw	17.6	17.3	17.5	17.4	17.5	-
CDi	122.7	122.4	122.4	122.2	122.1	-
CDsp	0.8	0.2	0.0	0.0	0.0	-

Based on Table 3 and Fig. 8, several remarks can be made:

1) The pressure drag coefficient shows more variation at CL = 0.58 and Re 5 million: 8.4 drag counts between the Tiny and Extra Fine grids (as already mentioned, critical convergence issues encountered with the Ultra Fine grid at this Reynolds number) versus 4.8 counts at Re 20 million between the Tiny and Ultra Fine grids. Also considering the CDp curve from DPW-6, it could be concluded that greater lift level conditions above the design point require finer grids, especially at low Reynolds numbers. And at a given CL, increasing Re seems to reduce the pressure drag prediction sensitivity to grid refinement. Concerning the absolute values, CDp converges to about 178 counts at Re 20 million, which is in good agreement with the average of DPW-7 participants, and around 198 counts at Re 5 million, exhibiting 20 d.c. of difference due to the Reynolds number increase at CL = 0.58. A dedicated part of the article will deal with the analysis of Reynolds effects.

2) The friction drag variation is almost non-existent in all cases: it was expected but it confirmed that using grids designed for higher Reynolds numbers was eventually not an issue in terms of accuracy even with finest grids at Re 5 million. At CL = 0.58, this coefficient goes from around 113 to 94 counts with the Reynolds increase, which is consistent with previous investigations of the authors [3].

3) The far-field coefficients in Table 3 allow the different drag contributions at higher Reynolds number than previously (20 versus 5 million) and greater lift level (0.58 versus 0.5) to be highlighted. The viscous pressure component, part of the viscous drag which is not friction, converges to about 38 counts, i.e. 14% of total drag while the friction coefficient represents 34%. The wave drag, extremely limited at the design point, weighs here more than 6% and the lift-induced drag, strongly growing with the lift increase, 45% of total drag.

The very low levels of spurious drag demonstrate the good quality of the grids used in this study for drag prediction.

4) The pitching moment *CM* shows a variation of about 0.004 between the Tiny and Ultra Fine grids at *Re* 20 million. As for the *CDp* coefficient, the variation is more important at *Re* 5 million (close to 0.006). The CM values obtained, about -0.0126 for *Re* 20 million, are here again in satisfactory agreement with the results of other DPW-7 participants. However, as it was highlighted since DPW-6 [7], the CFD pitching moment seems to be overestimated (too negative) because of an excessive aft-loading prediction compared to the experiments.

This leads to the following local analyses showing in Fig. 9 the pressure distributions on 4 sections of the wing at *CL* close to 0.58 and *Re* of 5 and 20 million. In this figure, experimental results from the National Transonic Facility of NASA (NTF) are given [10,27]. It can be noticed that at least in the sections located at 28.3, 50.2, and 72.7% of span the agreement between numerical and experiments is globally good for both Reynolds numbers. With the *Re* increase, the lift is slightly reduced before the shock, and increased after, the shock itself being shifted a bit more downstream.

And as evoked, the RANS CFD tends to over-predict the lift in the rear part of the wing profile, generating a too strong nose-down pitching moment compared to the wind tunnel data. It seems that no clear answer has emerged from the Workshop about this issue. The methods which include a coupling with a boundary layer code could possibly give better results in this area.

Another aspect concerns the significant differences that can be seen between numerical and experimental data in the most external wing section at 95% span (first part of suction side). This was not visible at *CL* = 0.5 in DPW-6 [6]. The same differences are observed with the kω-SST model and even in URANS computations. Several reasons can be proposed to explain this unusual disagreement but without absolute certainty: flow instabilities at wingtip with potential shock or boundary layer / vortex interactions, local deformation of the model geometry, issues in the *Cp* wind tunnel measurements (in Fig. 9, one triangle symbol at *Re* 5 million is far from the others and matches the CFD curve).

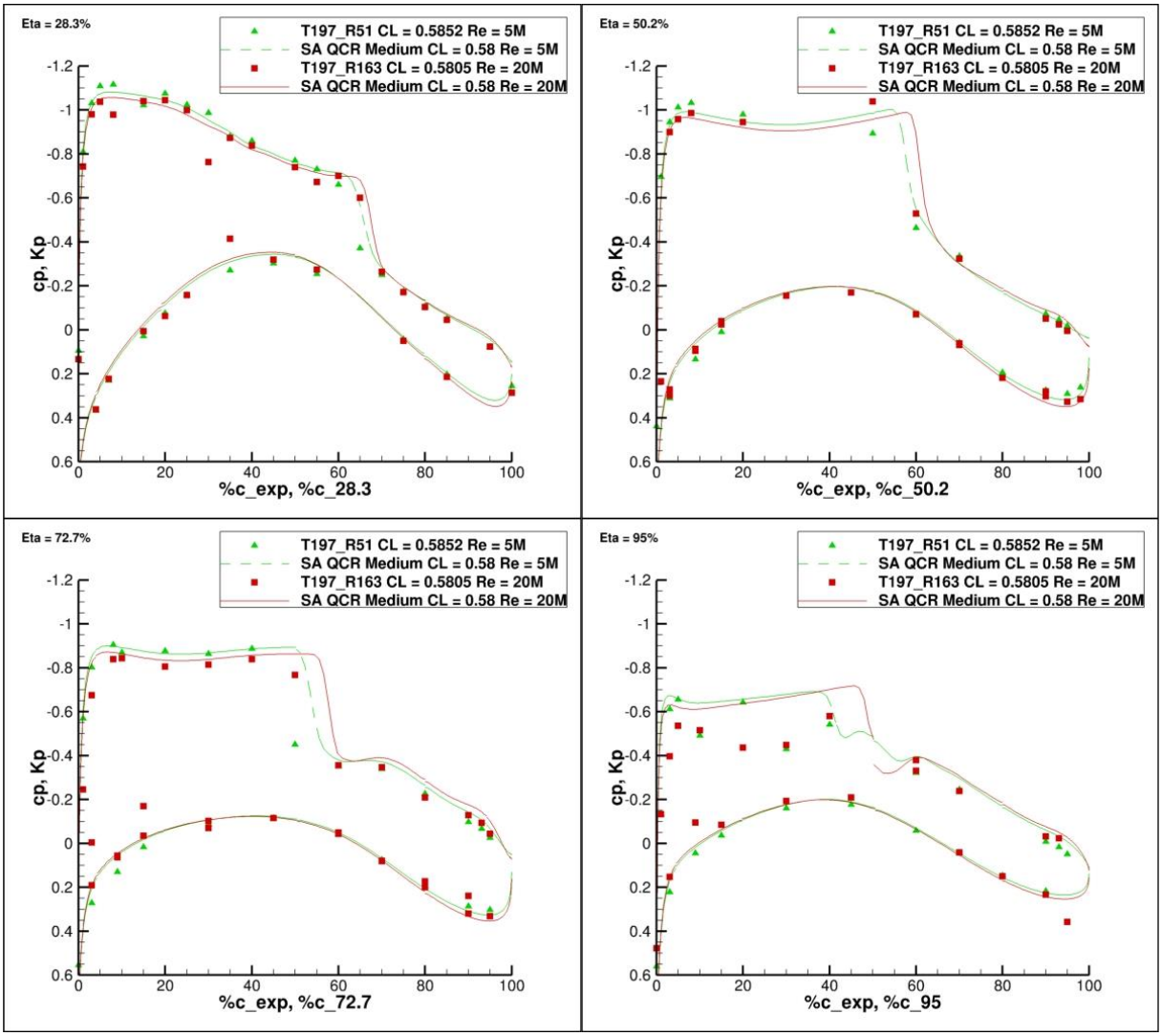

Fig. 9 WB; *Ma* = 0.85, *Re* = 5 and 20 x 10^6, *CL* ~ 0.58; wing pressure distributions.

V. The Angle of Attack Sweep Study

For the *AoA* sweep study the Medium grids corresponding to 2.50°, 2.75°, 3.00°, 3.25°, 3.50°, 3.75°, 4.00°, and 4.25° wing geometries (A250 to A425) are used. Each grid defines the wing geometry as it was measured in the wind tunnel for the specified Angle of Attack. This method allows the aero-elastic deformations to be taken into account as it would be the case in a coupled aero-structure computation. The Mach and Reynolds numbers are unchanged.

A. Lift, Drag, and Pitching Moment Polars

First, Fig. 10 shows the lift polar at *Re* 5 and 20 million for two turbulence models: SA and kω-SST, both used with the QCR-2000 approach. No *CL* drop is observed in this *AoA* range. A slight slope break can be seen around 3.25° with the SA model, closer to 3.00° with the kω-SST model but even slighter. The model effect is really significant at both Reynolds numbers: SA produces a much greater lift for a given *AoA*, for instance + 0.0175 at 3.25° and *Re* = 20 million. Nevertheless the Reynolds effect itself is consistent between the two models. It is relatively constant over the whole polar: about + 0.037 for *CL* due to the *Re* increase from 5 to 20 million.

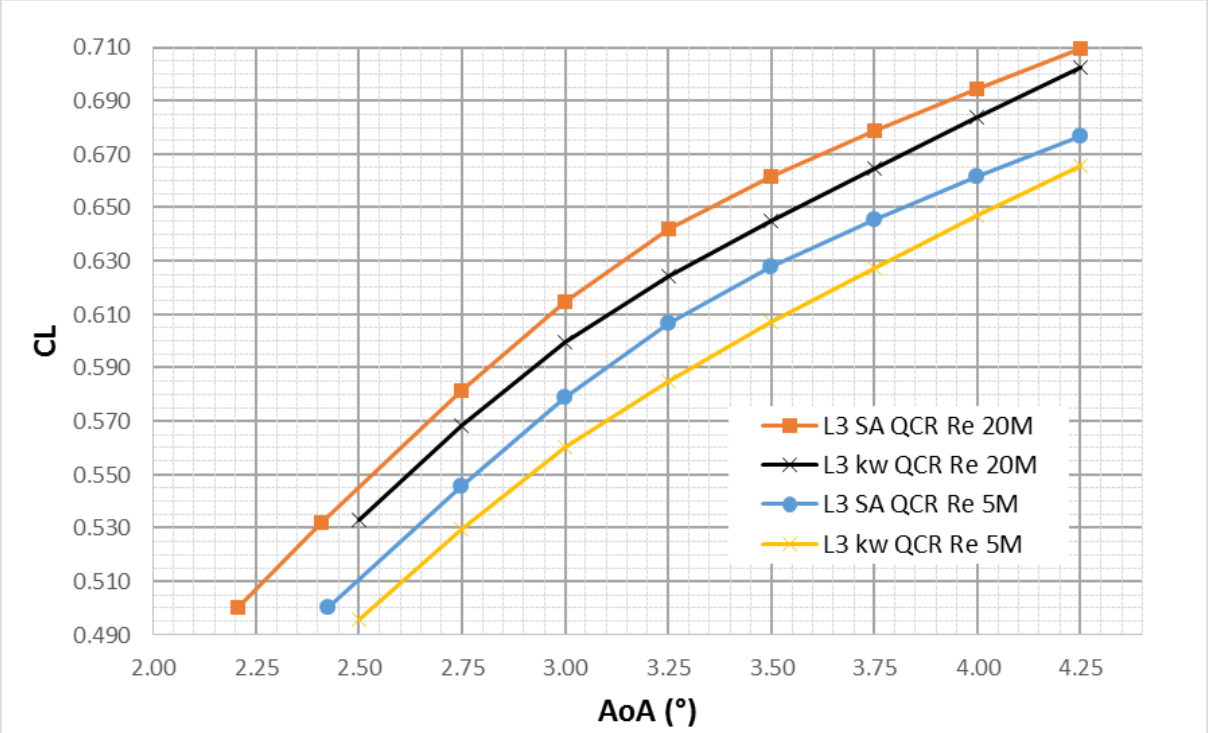

Fig. 10 WB; *Ma* = 0.85, *Re* = 5 and 20 x 10^6; Medium grids; lift polar.

Then, Fig. 11 gives the drag polar with the same set of data as in the previous figure but some DPW-6 numerical results are added as well as experimental data from NASA-NTF [10,27] and ONERA-S1MA [28]. Here again the differences between the SA and kω-SST models are significant, especially for the lowest Reynolds number. A delta up to about 30 drag counts can be observed in iso-*CL* conditions, which is clearly not a negligible difference even at such high lift and drag levels. This is more than the grid effect which can be quantified between the DPW-7 point-matched grid computations and the DPW-6 Overset grid results, both performed with the SA QCR-2000 model.

Indeed, if a good agreement does exist at *CL* = 0.50 as demonstrated in Table 2, this is no longer true for greater lift coefficients and differences up to 20 counts are visible. It highlights the increased sensitivity to grid and model in aerodynamic conditions beyond the design point. About the Reynolds effect between 5 and 20 million, for both models it increases with the lift level, from around -30 drag counts at *CL* = 0.5 with the SA model to more than -80 d.c. for *CL* close to 0.68.

Without diving too deeply into the topic of CFD / wind tunnel comparisons of absolute integrated coefficients, it can be said that the two experimental curves in Fig. 11 illustrate some of the difficulties of this exercise. First, one can think that at least for *CL* up to 0.61 the agreement is rather satisfactory between the DPW-7 SA results and the NTF data. Nevertheless, this experimental polar is not corrected from support system effects [29] and it has been shown in Fig. 35 of [28] that when looking at the whole drag polar from negative to high lift levels, a good agreement can be seen close to *CL* = 0.5 but nowhere else, simply because the numerical and experimental curves cross at this point. On the other hand, when some additional corrections are applied to the wind tunnel data, for example considering the S1MA polar which does take into account the support system effect, it can be noticed that substantial differences may remain between the CFD and experimental absolute values. And the possible reasons for that are always abundant. Of course, the sting effect correction might be imperfect, but it could also be a difference in geometry since the NASA and ONERA CRM models are not identical, especially considering their reaction to loading.

As briefly suggested in [28] and more recently better explained in [30] on a simpler case, the roughness might be an interesting parameter to propose more accurate comparisons between numerical and experimental worlds. Almost all computations, except for icing issues, are carried out on perfectly smooth surfaces, this is not the case in the wind tunnel. And the effect of model roughness seems to become more important when lift levels increase, which is consistent with what is observed in Fig. 11.

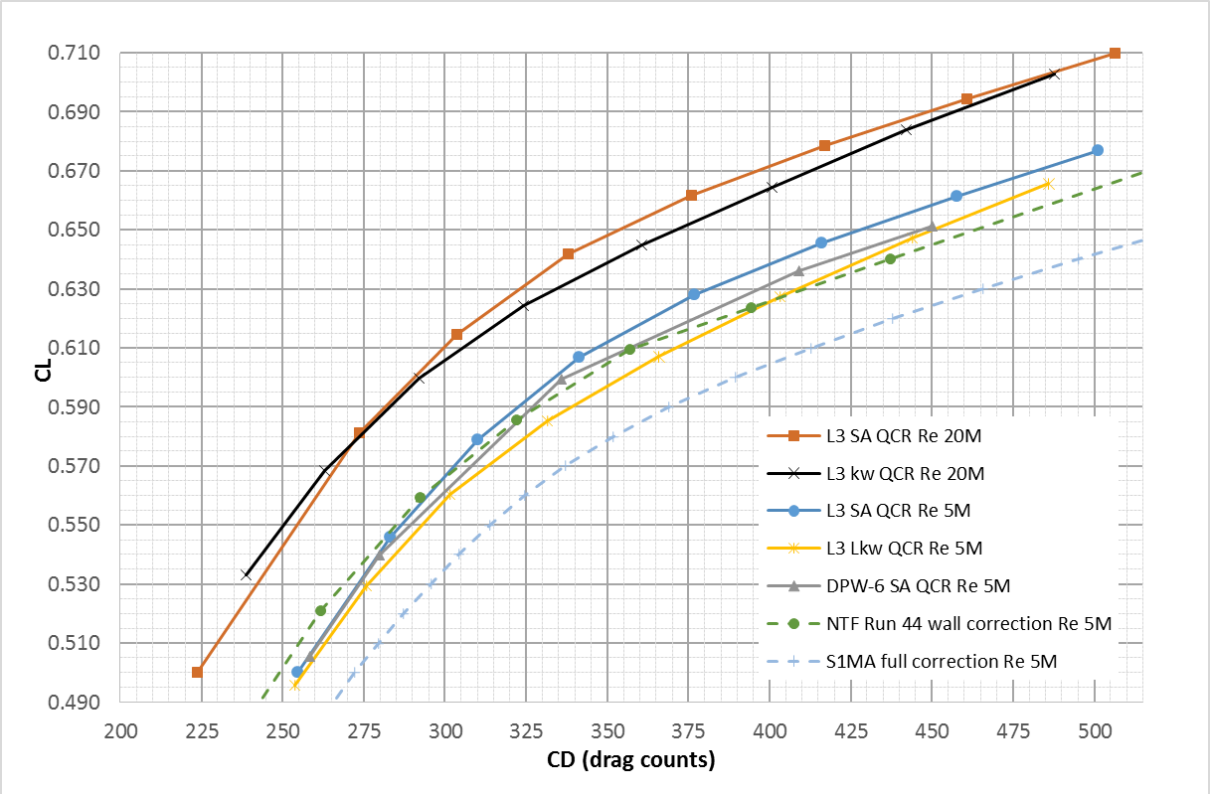

Fig. 11 WB; *Ma* = 0.85, *Re* = 5 and 20 x 10^6; Medium grids; drag polar.

Concerning the pitching moment, Fig. 12 shows the results with the SA and kω-SST models. The issue of the numerical aft-loading overestimation makes the comparison with the wind tunnel data difficult: the *CM* from CFD is much more negative. Besides, the difference between the turbulence models is substantial. For example, 0.013 of difference between SA and kω-SST at *CL* = 0.58 for *Re* 20 million, and 0.015 at *Re* 5 million, this is more than 10%. The pitch break is also not predicted at the same lift level: it appears significantly earlier with the kω-SST model, 0.60 versus 0.64 at the highest Reynolds number. However, both models are in relatively good agreement for the Reynolds effect. As for drag, the effect on pitching moment increases with the lift level (more clearly with the SA model). At *CL* = 0.58, switching from 5 to 20 million leads to a *CM* change of about -0.021 to -0.023. And the pitch break is delayed at *Re* 20 million (+ 0.03 to 0.04).

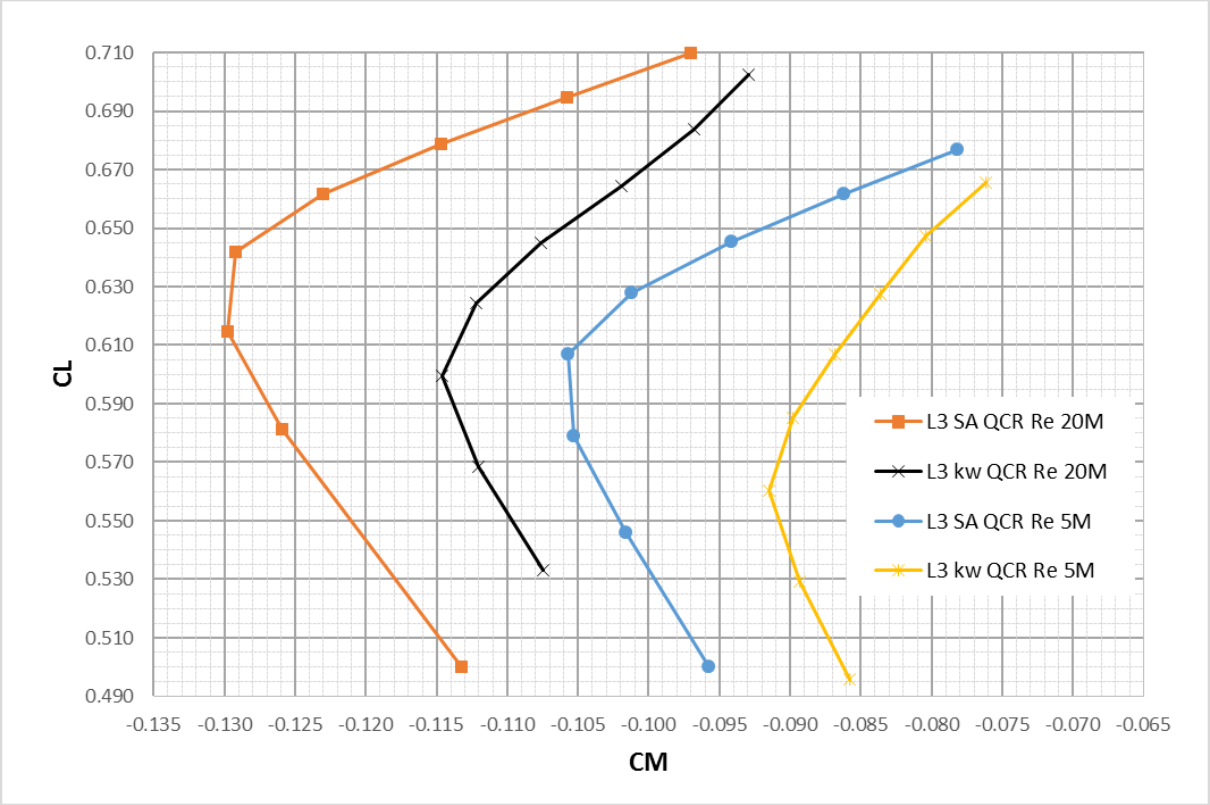

Fig. 12 WB; *Ma* = 0.85, *Re* = 5 and 20 x 10^6; Medium grids; pitching moment polar.

B. Flow Separation at High *AoA*

A focus is given here on the flow separation affecting the wing when the Angle of Attack increases beyond the cruise conditions. To begin, the advantage of the QCR approach is reminded in Fig. 13 at 4.25° and *Re* 5 million. As it was demonstrated in DPW-6 [6], without this correction the solver predicts a too large flow separation at the Wing-Body junction, which generates *CL* drops that are not observed in the experiments.

In Fig. 14 at *Re* 20 million, it can be observed that the flow separation predicted by the SA model is larger than the one of the kω-SST. But this comparison is carried out in iso-*AoA* conditions, not in iso-*CL* conditions, and as shown in Fig. 10 the kω-SST model produces a lower lift coefficient for a specified *AoA*. Considering Fig. 12, in iso-*CL* conditions, the kω-SST model would likely predict a greater flow separation explaining the earlier pitch break. Also, by comparing Fig. 13 and Fig. 14 it is noticed that the flow separations of the SA model are similar between the two Reynolds numbers, but once again in iso-*AoA* conditions, meaning that in iso-*CL* conditions the flow separation of the highest *Re* would be smaller.

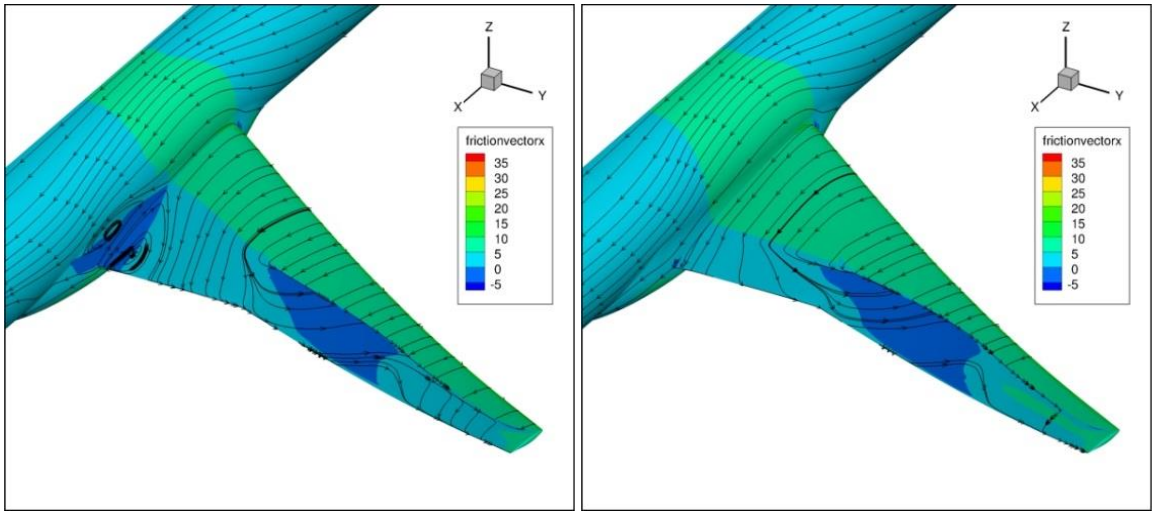

Fig. 13 WB; *Ma* = 0.85, *Re* = 5 x 10^6, *AoA* = 4.25°; SA (left) vs SA QCR-2000 (right).

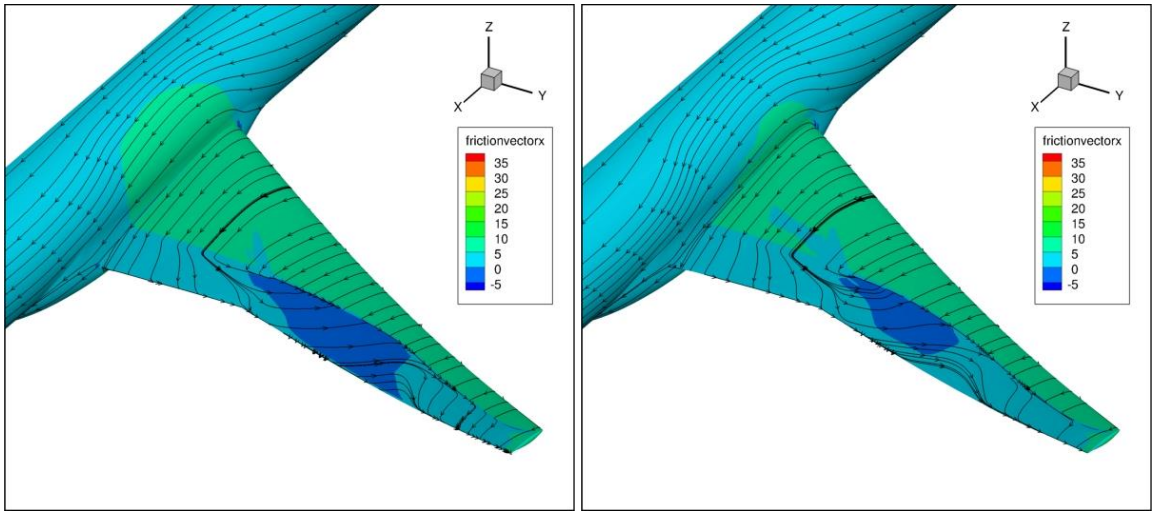

Fig. 14 WB; *Ma* = 0.85, *Re* = 20 x 10^6, *AoA* = 4.25°; SA QCR-2000 (left) vs kω-SST QCR-2000 (right).

Finally, Fig. 15 presents the flow separation evolution from 3.00 to 4.00 degrees at *Re* 20 million with the SA model only. At 3.00°, the shock-induced separation is barely noticeable, but at 3.25°, *AoA* at which the slope break is visible in Fig. 10, its extent is no longer negligible.

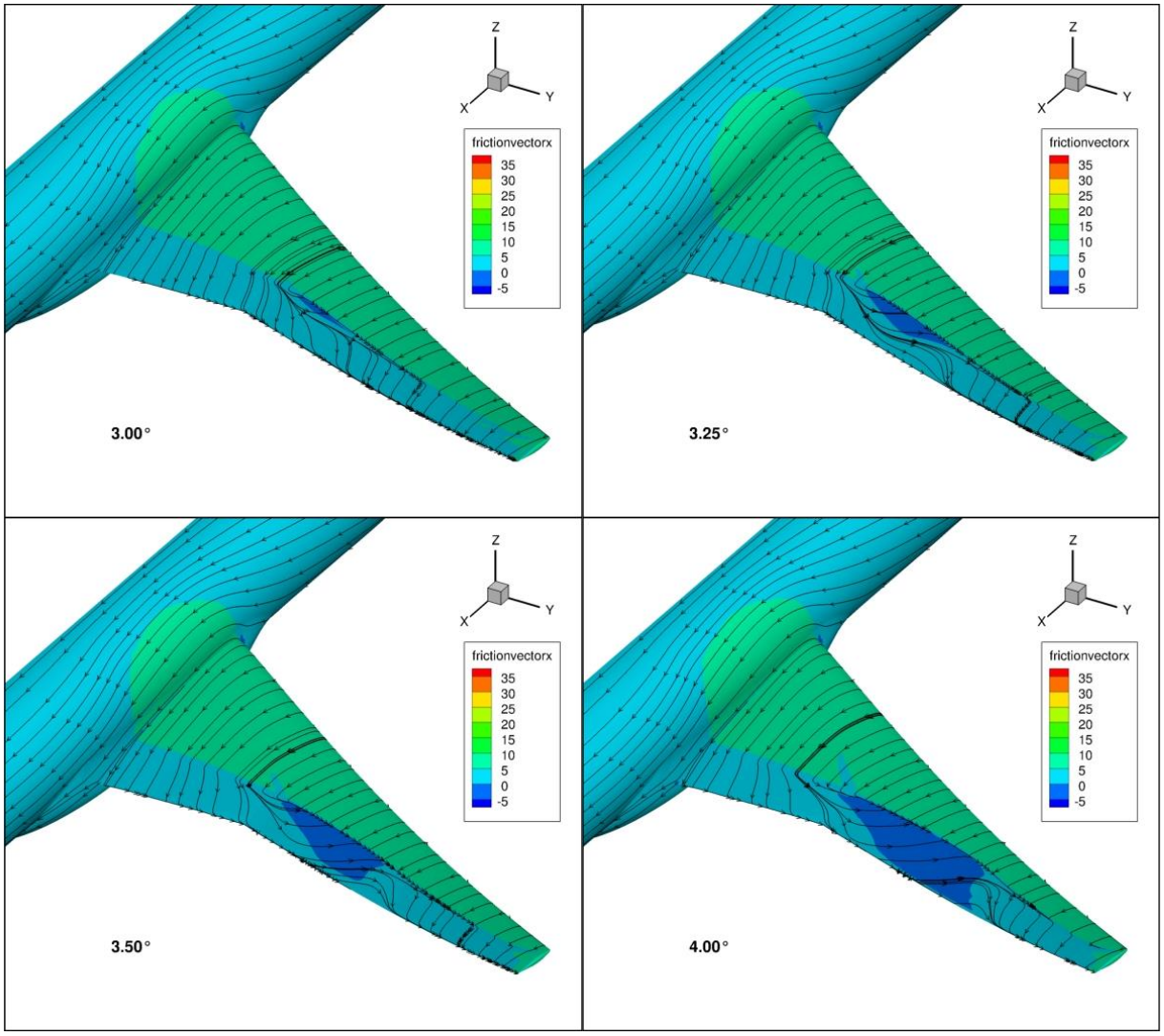

Fig. 15 WB; *Ma* = 0.85, *Re* = 20 x 10^6, *AoA* from 3.00° to 4.00°; SA QCR-2000.

VI. Reynolds number effects

Even if this topic is discussed along the whole paper, the present section is dedicated to the analysis of the Reynolds number effects, and especially at the cruise lift coefficient. Two geometries are used. The first one corresponds to the low dynamic pressure conditions for an *AoA* of 2.50° (A250), this is the same as in the *AoA* sweep study. The second one is also for 2.50° but in HiQ conditions, where the stagnation pressure is increased to simulate higher Reynolds numbers. The grids have Medium refinement levels in both cases. Consequently, the computations are carried out at *CL* = 0.5, *Ma* = 0.85, and *Re* = 5 and 20 million (LoQ geometry), plus 20 and 30 million (HiQ geometry). For a given geometry, the Reynolds number increase is mostly obtained by a drop in stagnation temperature (cryogenic).

A. Global Coefficients and Comparison to Experiments

The integrated coefficients are studied with near-field and far-field approaches and the numerical increments due to Reynolds number variations are compared to the wind tunnel polars shown in Fig. 16 (analysis of NTF data, courtesy of Edward Tinoco). The following profile drag variable needs to be introduced here and could be defined as the total drag minus an estimation of the lift-induced drag, which leaves the viscous and wave drag contributions:

$$CD_{profile} = CD_{nf} - CL^2/(\pi * AR) \quad \textbf{(6)}$$

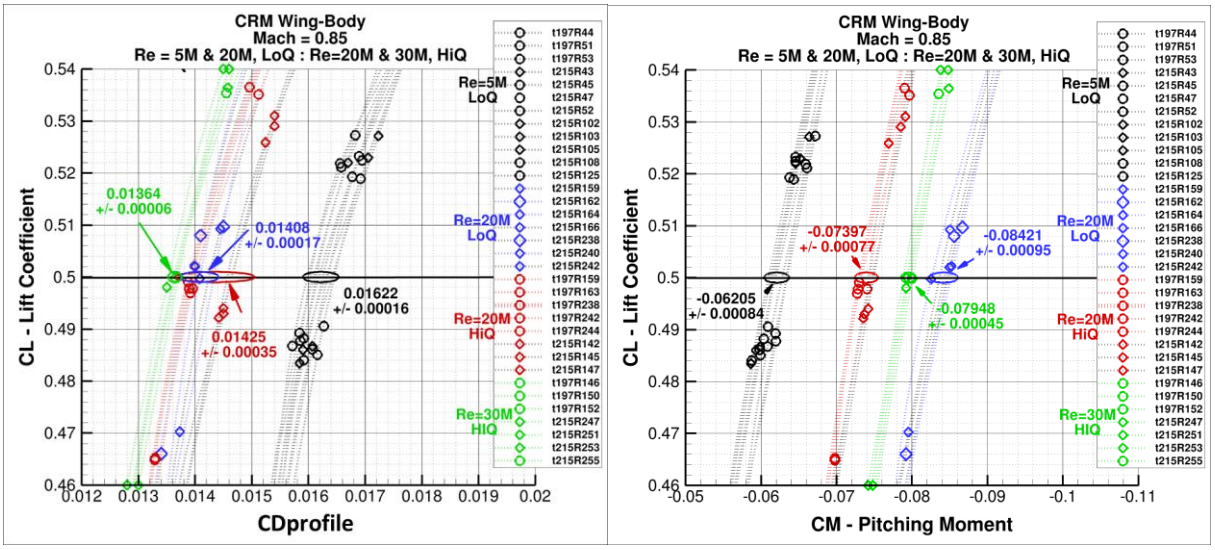

Fig. 16 WB; *Ma* = 0.85, *Re* = 5, 20, and 30 x 10^6; Reynolds effect from NTF (courtesy of Edward Tinoco).

Fig. 16 gives the profile drag and pitching moment according to the lift coefficient close to *CL* = 0.5. The four conditions in terms of *Re* and dynamic pressure are highlighted. Table 4 uses these figures and compares them to the numerical results. It was chosen to take the *Re* 30 million case as reference and to present all the differences with respect to this last column. Instead of the absolute values which are, as already said, tricky to compare between the numerical and experimental data, the deltas are analyzed.

1) Concerning the pitching moment, the CFD and wind tunnel increments are consistent, especially for the difference between the 20 and 30 million Reynolds number HiQ cases. But the agreement of deltas is not so good for the other columns. In particular the difference between the first (*Re* 5 million) and last columns (*Re* 30 million) shows a much greater value in the experimental case: + 0.01743 when switching from 30 to 5 million versus 0.0096. This can probably be explained, at least partially, by the characteristics of the wind tunnel tests and will be described below about the drag.

2) The global effect of increasing the Reynolds number is a drag reduction. In HiQ conditions, going from 20 to 30 million leads to a near-field drag decrease of 7,6 counts, and between 5 and 20 million at iso-geometry about 31 counts. The difference between the two computations at *Re* = 20 million is due to the geometry but it is very limited, mainly on the wave drag (1.2 d.c.). These drag reductions at higher Reynolds number are obviously driven by friction drag decreases, about 60% in the present cases, but not only. The wave drag is also slightly reduced and the viscous pressure drag component is responsible for about 30% of drag reduction (reduced boundary layer thickness). Focusing on the profile drag and the comparisons to experiments, it can be said that the agreement is satisfactory for the deltas between the cases at *Re* = 20 and 30 million (4.4 d.c. versus 4.7 and 6.1 d.c. versus 7.6). However, as with the pitching moment, the agreement is no longer good with the 5 million *Re* case. For the drag, it seems that the numerical difference is overestimated: 35.7 counts versus 25.8. Taking the same geometry at *Re* 20 million as the reference instead of the one at 30 million gives deltas of 31 and 21.4 counts for the CFD and wind tunnel data respectively, the disagreement is almost the same. Two parameters of the wind tunnel campaign could be highlighted to understand this issue. It is useful to observe the absolute values: the CFD produces a greater profile drag at the lowest Reynolds number compared to the experiments, and on the other hand lower drag levels at higher *Re*. First, the computations are fully turbulent whereas the tests include lines of Cadcuts at 10% chord (transition tripping device). At *Re* = 5 million, the flow may remain laminar up to the Cadcuts and therefore the drag is reduced [5]. Then, as already mentioned, the computations are carried out with perfectly smooth surfaces, which is not the

case in the real world of experimental tests. The model roughness might induce a larger drag at higher Reynolds numbers, indeed with the boundary layer height reduction the same roughness can start to generate non-negligible effects. These two hypotheses combined could justify why the RANS-based CFD gives greater drag coefficients at smallest *Re* and lower ones at highest *Re* compared to wind tunnel data, explaining the strong numerical Reynolds effect of the first column.

Table 4 WB; *Ma* = 0.85, *Re* = 5, 20, and 30 x 10^6, *CL* = 0.5; global coefficients

	Re 5M LoQ	Re 20M LoQ	Re 20M HiQ	Re 30M HiQ
Alpha (°)	2.425	2.205	2.385	2.330
CM	-0.0957	-0.1132	-0.1007	-0.1053
Exp data CM (Average)	-0.06205	-0.08421	-0.07397	-0.07948
Delta Num CM / Re 30M	0.0096	-0.0079	0.0046	0.0
Delta Exp CM / Re 30M	0.01743	-0.00473	0.00551	0.0
CDnf	254.8	223.8	226.7	219.1
CDprofile	166.4	135.4	138.3	130.7
Exp data CDprofile (Average)	162.2 +/- 1.6	140.8 +/- 1.7	142.5 +/- 3.5	136.4 +/- 0.6
Delta Num CDprofile / Re 30M	35.7	4.7	7.6	0.0
Delta Exp CDprofile / Re 30M	25.8	4.4	6.1	0.0
CDp	140.6	128.3	131.4	128.5
CDf	114.2	95.5	95.3	90.6
CDvp	42.2	32.7	33.0	30.7
CDv	156.4	128.2	128.3	121.3
CDw	6.1	4.1	5.28	4.8
CDi	92.4	91.6	93.2	93.0

B. Local Analyses

In this sub-section, the effects of Reynolds number and dynamic pressure variations are investigated through spanwise distributions of viscous pressure drag (Fig. 17) and wave drag (Fig. 18).

Regarding the viscous pressure drag production along the wing span, it can be noticed that, at *Re* = 20 million, switching from LoQ to HiQ conditions does almost not change the spanwise distribution of *CDvp*. On the contrary, at fixed dynamic pressure, *CDvp* decreases as expected when increasing *Re* (from 5 to 20 million in LoQ conditions, from 20 to 30 million in HiQ conditions) due to the weakening of viscous effects.

Concerning the wave drag production along the wing span, it can be seen that contrary to the viscous pressure drag, switching from LoQ to HiQ conditions at *Re* = 20 million does yield an increase in *CDw* due to a stronger

wing loading in this case. When increasing *Re* for a fixed dynamic pressure, *CDw* actually decreases, probably due to the fact that it is necessary to decrease the angle of attack in order to stay at *CL* = 0.5.

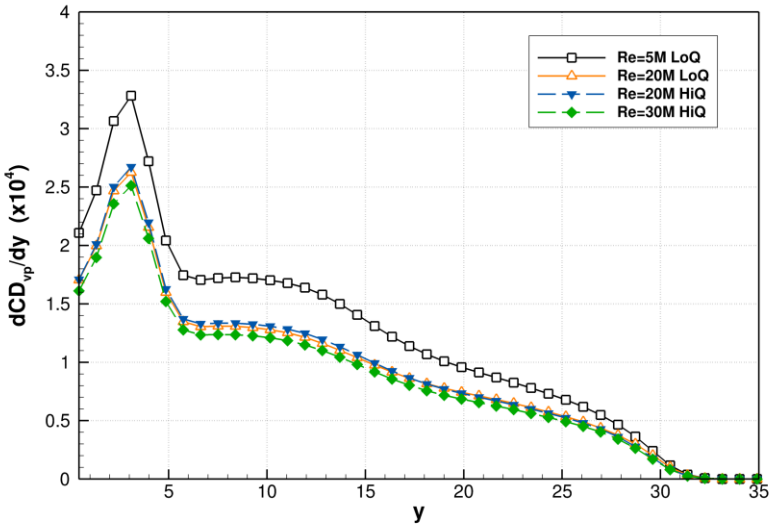

Fig. 17 WB; *Ma* = 0.85, *Re* = 5, 20, and 30 x 10^6, *CL* = 0.5; *CDvp* production along span.

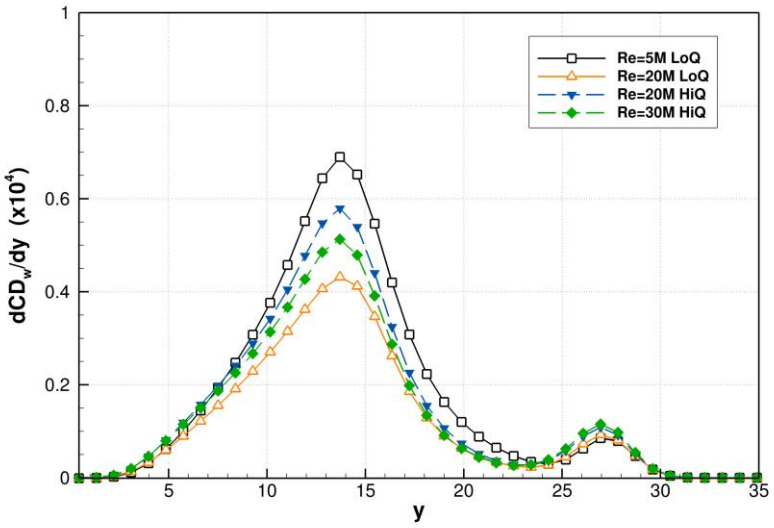

Fig. 18 WB; *Ma* = 0.85, *Re* = 5, 20, and 30 x 10^6, *CL* = 0.5; *CDw* production along span.

VII. URANS computations

In this section, results of the time-accurate simulations are presented. This work corresponds to the optional test-case "Beyond RANS" of the Workshop, in which the participants were invited to use alternative methods to analyze the flow at high *AoA* and possibly buffet phenomenon for a Reynolds number of 20 million. ONERA opted for URANS simulations since this approach can provide an accurate description of the unsteadiness of the shock wave while keeping the cost of the simulation reasonable, as it has been demonstrated in many 3D configurations, from simple extruded profiles [31] to more complex wind-body configurations [32]. A complete review summarizing the progress made in the past years, including the capabilities of URANS simulations has recently been published [33]. Contrarily to high-fidelity methods such as DNS or Z-DES, URANS is able to provide useful information about the unsteady dynamics of the flow in buffet conditions in a short amount of time and with limited resources. However, the turbulence remains completely modelled as for the steady-state RANS simulations and only the large-scale unsteadiness can be reproduced.

Since one of the objectives of this study was to provide information about how the URANS method compares with the steady-state results described in the previous sections, all the numerical parameters of these simulations were exactly the same as the RANS simulations with the SA turbulence model, QCR, and Jameson scheme. The only difference is that the time algorithm is changed from backward-Euler to Gear, providing a global time stepping instead of a local one.

The choice of the time step is the first question that has been addressed. A convergence study was carried out, starting from the converged RANS solution, using different time steps. At the beginning, the Tiny grid was used in order to have a quick estimation of the buffet phenomenon, localize the position of the unsteadiness on the wing, the intensity and, most importantly, the buffet period. The illustration on the left of Fig. 19 shows a result of a time-accurate simulation at *AoA* = 4.25° on the Tiny grid. The distribution of pressure is shown, superposed to the corresponding grid. While the y^+ discretization is sufficiently fine (0.4) and the buffet phenomenon can be reproduced with shock motions observed on the wing, the spanwise spatial discretization in the buffet region is too coarse to validate the result. According to the data obtained with this Tiny grid, the buffet phenomenon has a frequency of 5.90 Hz. For this case, a time step of 1×10^{-4} seconds, corresponding to 1700 steps per buffet period, was sufficient to reproduce the phenomenon. However, as it can be seen on the right of Fig. 19, presenting the time

evolution of the lift coefficient for the Tiny, Coarse and Medium grids at the same angle of attack, the buffet frequency of the Tiny grid is much lower than the ones observed in the other cases. It can thus be concluded that the Tiny grid can reproduce the main features of buffet, despite poor spanwise discretization, but the unsteady behavior of the shock wave might not be correctly captured.

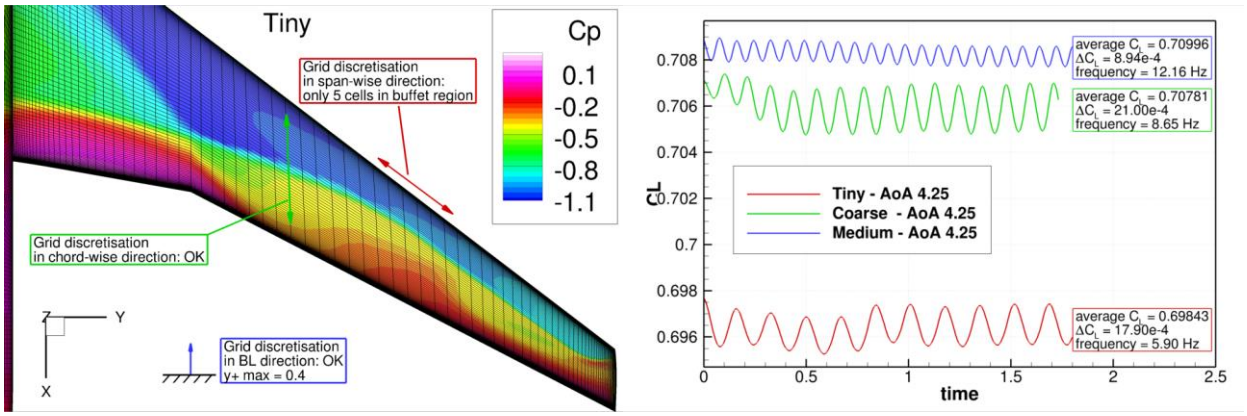

Fig. 19 Left: instantaneous *Cp* distribution at *AoA* =4.25° on the Tiny grid. Right: comparison of the time-history of the lift coefficient for different grids during a URANS simulation.

From the time history of the lift coefficient in Fig. 19, it can be seen that the grid refinement has an impact not only on the buffet frequency, but also on the average value of the lift coefficient and the amplitude of the shock motions. The impact on the lift level is also observed in RANS computations, it is expected that with several grids of very different refinements, the associated calculations all performed at a given *AoA* will produce different *CL* coefficients. Concerning buffet, while it seems reasonable to imagine that the Medium grid has the most accurate result, it is not possible to draw a conclusion without comparisons with some experimental data, unfortunately not available. As it was described in previous studies [34], sometimes a too fine spatial discretization on the wing can mitigate the shock buffet intensity: this could be the case for the Medium grid.

The three images in Fig. 20 show the distribution of the pressure fluctuations obtained by the URANS simulations performed in the same aerodynamic conditions on the three grids. A logarithmic scale in the color-map is presented, with the blue color indicating no unsteadiness, while the red indicates the strongest pressure fluctuations over one buffet period. The images are obtained by time-averaging the solution, after the transient regime. While some differences can be seen between the results obtained on the Tiny grid and the others, the fluctuations obtained with the Coarse and Medium grids are almost identical: most of the pressure fluctuations are located at the shock foot, outboard of the crank, with intensities rising up to more than 160 Pa. Downstream of the

shock foot, an unsteady separation is responsible for pressure fluctuations between 50 and 160 Pa. This region corresponds to the location of the buffet unsteadiness: the fact that the separated zone is slightly shifted towards the wingtip with respect to the location of the most energetic shock unsteadiness can be explained by the convection of the separated zone towards the outboard of the wing.

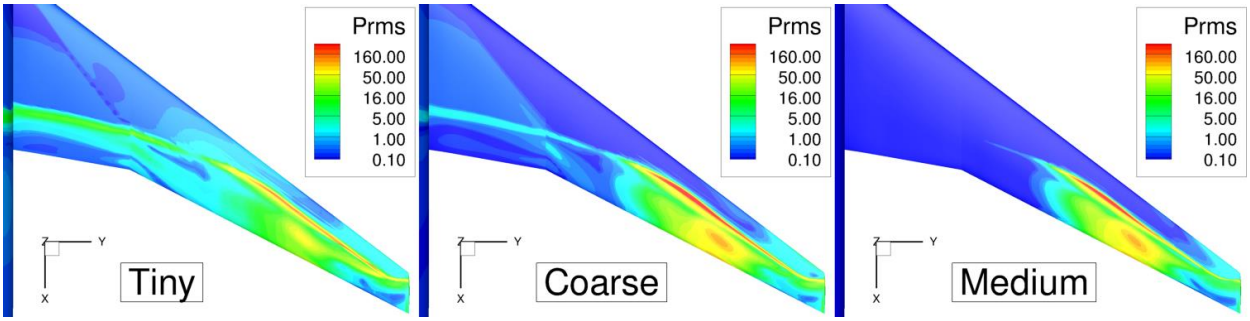

Fig. 20 Comparison of the root mean square of pressure distributions for different grids.

The Medium grid has then been selected for the remainder of the study. Thanks to the data available in the workshop, the simulations performed on this grid take into account the wing deformation for each *AoA* considered. The simulations presented below were performed on 384 cores, distributing the simulation on more processors than in the RANS case, however without doing an additional grid splitting. Due to a long transient regime, it was necessary to simulate at least 10 buffet periods before obtaining a statistically converged solution. Thus, roughly 100 physical hours were needed for a complete simulation. Three angles of attack were considered for this grid: 2.755°, corresponding to CL = 0.58, 4.00° and 4.25°. The three images in Fig. 21 present a comparison of the pressure fluctuations obtained with these three angles of attack. As presented in the images in Fig. 20, the color-map has a logarithmic scale, allowing for broad comparison of pressure fluctuations.

On the left side of Fig. 21, very low values of pressure fluctuations indicate that the flow is steady at this relatively low angle of attack. Very small fluctuations can be observed on the shock foot, but without any link to a buffet phenomenon.

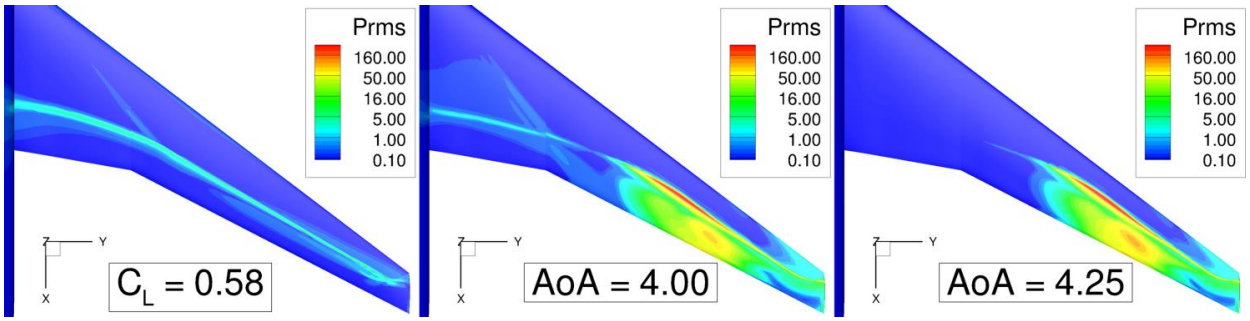

Fig. 21 Pressure fluctuations on the Medium grid for different angles of attack.

In the center of Fig. 21, the pressure fluctuations at *AoA* = 4.00° show that the flow is in buffet conditions. However, contrary to what is observed on the right side of Fig. 21, where the simulated *AoA* is 4.25°, some unsteadiness can be observed in the inner part of the wing, where the so-called "Lambda shock foot" is visible because of the interaction between the wing and the fuselage. The frequencies of the buffet phenomenon observed when the *AoA* is 4.00° and 4.25° is 11.9 Hz and 12.2 Hz, respectively. These values correspond to a Strouhal number St = 0.464, in fair agreement with what was found by Paladini et al. [35] on a similar configuration. In their work, Paladini et al. analyzed the experimental data issued from a European project called FLIRET (contract number AIP3-CT-2003-502773, funded by the European Commission), carried out in 2005 in the ETW, over a half wing-body configuration. The model, designed by Airbus UK, was aimed at representing a typical Airbus passenger airplane with a supercritical airfoil and a double sweep at the trailing edge, similarly to the CRM considered in this study. The FLIRET model has also been tested in flow conditions beyond cruise and at high Reynolds number: during the experimental investigation the Strouhal number based on the mean aerodynamic chord for the FLIRET geometry was St = 0.48. Then, concerning the values of lift coefficient (averaged over multiple buffet periods), the increase of the angle of attack from 4.00° to 4.25° corresponds to an increase of *CL* from 0.69476 to 0.70996. This result is very similar to what was obtained using steady-state simulations, as can be seen from Fig. 10, indicating that the RANS solution is here able to predict correctly the average value of time-accurate simulations. In this respect, it is worth mentioning that no difference between RANS and URANS solutions is observed in the case *CL* = 0.58, indicating that in the absence of unsteadiness, both RANS and URANS simulations yield the same solution.

Finally, a brief time-step convergence study has also been conducted for *AoA* = 4.25°, not only by varying the time-step size, but also changing the number of inner iterations between two time-steps. The analysis indicated that all time-steps between 1 x 10^{-5} s and 5 x 10^{-5} s associated with both Gear and DTS time-schemes (implicit Dual Time

Stepping method), both consisting in sub-iterating each time step for inner convergence, can produce a satisfactory solution, provided that a sufficient number of inner iterations is performed, in order to achieve convergence in the inner iterations.

VIII. Conclusions and perspectives

This article is aimed at presenting the studies led at ONERA in the framework of the 7th AIAA Drag Prediction Workshop. The objective of this new workshop has been to extend the envelope: first the grid convergence study is carried out in off-design conditions with a greater lift level, then the Reynolds number is increased with computations not only at 5 million but also at 20 and 30 million.

The geometry studied is still the CRM configuration, here in its Wing-Body version, and the wing deformation due to the loading variation is taken into account with different geometries corresponding to the considered angles of attack. In the present work, the structured point-matched grids provided by John Vassberg have been used [13,14], they represent a large set of grids, with different refinement levels for the grid convergence study from about 5 to 221 million of points, and additional medium grids for the *AoA* sweep and Reynolds number effect studies.

It has been seen in the grid convergence test-case that the higher *CL* level, 0.58 instead of 0.5, implies larger pressure drag variation between the coarsest and finest grids. However, the Reynolds number increase, from 5 to 20 million, tends to reduce this variation. The effects of greater *CL* and *Re* on the different aerodynamic coefficients have been shown and the issue of excessive numerical aft loading already noticed in the previous workshops is still observed. It seems that no sure and definitive answer about this point has come during the workshop.

Then, the *AoA* sweep study has been the occasion of highlighting some grid and turbulence model effects. Indeed, for lift, drag, and pitching moment polars, significant differences are observed between the SA and kω-SST models and also between the point-matched grids and DPW-6 Overset grids. For the drag polar, these differences are particularly noticeable at the highest *AoA*. This underlines that even if great progress has been made since the first workshop in the early 2000s, CFD has still room for improvements. On the other hand, the QCR approach, already used in DPW-6, has demonstrated again its relevance at the greatest AoA to avoid the issue of too extended flow separation at the Wing-Body junction. Concerning the delicate matter of comparing the numerical and experimental polars, the overall agreement, which is not the agreement in a limited part of the polar, will require more time and effort probably on both sides. The wind tunnel data should include accurate corrections at least for wall and support system, whereas the CFD should add more experimental parameters in its computations, such as the model roughness, but also needs to tackle its known limitations, such as the ones mentioned in these conclusions.

The Reynolds number effect has been investigated with near-field and far-field analyses. This has allowed to show that the drag reduction due to the *Re* increase is as expected mainly due to the friction component (60%) but also significantly to the viscous pressure drag (30%). The different drag and moment increments related to the *Re* variations from numerical and experimental data have been highlighted, and it appears that the pitching moment prediction remains a challenging exercise. Perhaps the advances on this subject are not as satisfactory as they have been for the drag. Nevertheless, these computations and the associated tests have provided an insight into the CRM at Reynolds numbers much closer to the real flight conditions.

Concerning the time accurate simulations, it has been shown that the URANS approach is capable of predicting unsteady buffet phenomenon for *AoA* above 4.00°. Nevertheless, no unsteadiness was found for the *AoA* corresponding to the lift level of the grid convergence study *CL* = 0.58. And about the necessary refinement, while the Medium grid has been used to provide most of the results, coarser grids also have allowed some flow unsteadiness to be reproduced. Finally, it seems that the RANS calculations up to *AoA* = 4.25° were able to predict correctly the average coefficients of URANS simulations. However in order to validate these unsteady simulations with transonic buffet, time-accurate experimental results would be welcome in the future.

Finally, next steps can be taken in terms of physical analysis of the obtained CFD solutions around the CRM configuration. In this aspect, further investigations of the steady solutions presented in this article will be carried out with the far-field exergy balance method developed at ONERA [36]. In parallel, an analysis of the time-accurate simulations presented is planned by using a specific unsteady far-field drag breakdown formulation [37].

Acknowledgments

The authors thank the DPW Organizing Committee and especially John Vassberg for the grids and Ed. Tinoco for his analysis of the CRM experimental data. The studies presented in this article have been funded with general resources of ONERA.

References

[1.] DPW website, https://aiaa-dpw.larc.nasa.gov

[2.] *Journal of Aircraft*, Special Section: Drag Prediction Workshop, Vol. 51, No. 4, July.-August. 2014, pp. 1069-1343.

[3.] Hue, D., and Esquieu, S., "Computational Drag Prediction of the DPW4 Configuration Using the Far-Field Approach," *Journal of Aircraft*, Vol. 48, No. 5, Sept.-Oct. 2011, pp. 1658-1670.

[4.] Hue, D., "Fifth Drag Prediction Workshop: Computational Fluid Dynamics Studies Carried Out at ONERA," *Journal of Aircraft*, Vol. 51, No. 4, July.-August. 2014, pp. 1295-1310.

[5.] Hue, D., "Fifth Drag Prediction Workshop: ONERA Investigations with Experimental Wing Twist and Laminarity," *Journal of Aircraft*, Vol. 51, No. 4, July.-August. 2014, pp. 1311-1322.

[6.] Hue, D., Chanzy, Q., and Landier, S., "DPW-6: Drag Analyses and Increments Using Different Geometries of the Common Research Model Airliner," *Journal of Aircraft*, Vol. 55, No. 4, July–August 2018, pp. 1509-1521.

[7.] Tinoco, E. N., Brodersen, O., Keye, S., Laflin, K., Feltrop, E., Vassberg, J. C., Mani, M., Rider, B., Wahls, R. A., Morrison, J. H., Hue, D., Roy, C. J. Mavriplis, D. J., Murayama, M., "Summary Data from the Sixth AIAA CFD Drag Prediction Workshop: CRM Cases," *Journal of Aircraft*, Vol. 55, No. 4, July–August 2018, pp. 1352-1379.

[8.] Coder, J. G., Hue, D., Kenway, G., Pulliam, T., Sclafani, A. J., Serrano, L., Vassberg, J. C., "Contributions to the Sixth Drag Prediction Workshop Using Structured, Overset Grid Methods," *Journal of Aircraft*, Vol. 55, No. 4, July–August 2018, pp. 1406-1419.

[9.] Vassberg, J. C., DeHann, M. A., Rivers, S. M., and Wahls, R. A., "Development of a Common Research Model for Applied CFD Validation Studies," AIAA Paper 2008-6919, 2008.

[10.] Common Research Model website, http://commonresearchmodel.larc.nasa.gov/

[11.] ETW CRM campaign website, https://w3.onera.fr/ESWIRP-TNA-ETW-CRM-2014/

[12.] Hantrais-Gervois, J.-L., and Destarac, D., "Drag Polar Invariance with Flexibility", *Journal of Aircraft*, Vol. 52, No. 3 (2015), pp. 997-1001.

[13.] DPW-7 Vassberg grids, https://dpw.larc.nasa.gov/DPW7/Vassberg_Grids.REV00/

[14] Vassberg, J. C., “A Unified Baseline Grid about the Common Research Model Wing-Body for the Fifth AIAA CFD Drag Prediction Workshop,” AIAA Paper 2011-3508, 2011.

[15] CFD General Notation System website, http://cgns.github.io/

[16] Benoit, C., Péron, S., and Landier, S., “Cassiopee: A CFD pre- and post-processing tool,” *Aerospace Science and Technology*, Vol. 45, September 2015, pp. 272-283.

[17] DPW-7 Vassberg grids converted into CGNS files, https://dpw.larc.nasa.gov/DPW7/ONERA_Grids.REV00/

[18] Cambier, L., Heib, S., and Plot, S., “The ONERA *elsA* CFD Software: Input from Research and Feedback from Industry,” *Mechanics and Industry*, Vol. 15(3), pp. 159-174, 2013.

[19] Jameson, A., Schmidt, W., and Turkel, E., “Numerical Solution of the Euler Equations by Finite Volume Methods Using Runge Kutta Time Stepping Schemes,” AIAA Paper 81-1259, June 1981.

[20] Spalart, P. R., and Allmaras, S. R., "A One-Equation Turbulence Model for Aerodynamic Flows," AIAA Paper 92-0439, 1992.

[21] Menter, F. R., "Two-Equation Eddy-Viscosity Turbulence Models for Engineering Applications," *AIAA Journal*, Vol. 32, No. 8, August 1994, pp. 1598-1605.

[22] Spalart, P. R., "Strategies for Turbulence Modelling and Simulation," *International Journal of Heat and Fluid Flow*, Vol. 21, 2000, pp. 252-263.

[23] Destarac, D., “Far-Field / Near-Field Drag Balance Applications of Drag Extraction in CFD,” *CFD-Based Aircraft Drag Prediction and Reduction*, VKI Lecture Series 2003-02, von Karman Institute for Fluid Dynamics, Rhode-Saint-Genèse, Belgium, 3-7 November 2003.

[24] Van Der Vooren, J., and Destarac, D., “Drag/thrust analysis of jet-propelled transonic transport aircraft; definition of physical drag components,” *Aerospace Science and Technology*, Vol. 8, No. 6, 2004, pp. 545–556.

[25] Bailly, D., Petropoulos, I., Wervaecke, C., Méheut, M., Atinault, O. and Fournis, C., “An overview of ONERA research activities related to drag analysis and breakdown”, AIAA Paper 2021-2551, Virtual Event, 2021.

[26] Petropoulos I., Wervaecke C., Bailly D., and Derweduwen T., "Numerical investigations of the exergy balance method for aerodynamic performance evaluation," AIAA Paper 2019-2926, 2019.

[27] Rivers, M. B., Dittberner, A., “Experimental Investigation of the NASA Common Research Model (Invited),” AIAA Paper 2010-4218, 2010.

[28] Cartieri, A., Hue, D., Chanzy, Q., and Atinault, O., “Experimental Investigations on Common Research Model at ONERA-S1MA – Drag Prediction Workshop Numerical Results,” *Journal of Aircraft*, Vol. 55, No. 4, July–August 2018, pp. 1491-1508.

[29] Rivers, M. B., Hunter, C. A., and Campbell, R., L., “Further Investigation of the Support System Effects and Wing Twist on the NASA Common Research Model,” AIAA Paper 2012-3209, 2012.

[30] Hue, D., Molton, P., "Turbulent drag induced by low surface roughness at transonic speeds: Experimental/numerical comparisons," *Physics of Fuids*, Vol. 32, No. 4, 2020.

[31] Iovnovich, M., Raveh, D.E., "Reynolds-averaged Navier-Stokes study of the shock buffet instability mechanism", *AIAA Journal*, Vol. 50, No. 4, 2012, pp. 880-890

[32] Sartor, F. and Timme, S., "Reynolds-Averaged, "Navier-Stokes simulations of shock buffet on half wing-body configuration", AIAA Paper 2015-1939, 2015

[33] Giannelis, N., Vio, G., and Levinski, O., "A Review of Recent Developments in the Understanding of Transonic Shock Buffet", *Progress in Aerospace Sciences*, Vol. 92, 2017, pp. 3984

[34] Sartor, F., Martin, M., Riveiro Moreno, C., and Dandois, J., "Numerical Simulations of Transonic Buffet on Half Wing-Body Configuration," Presented at ICAS2020 conference, Shanghai, September 2021.

[35] Paladini, E., Dandois, J., Sipp, D., and Robinet, J.-Ch., "Analysis and Comparison of Transonic Buffet Phenomenon over Several Three-Dimensional Wings," *AIAA Journal* 2019 57:1, 379-396.

[36] Arntz A., "Civil aircraft aero-thermo-propulsive performance assessment by an exergy analysis of high-fidelity CFD-RANS flow solutions", Ph.D. Thesis, Lille 1 Université - Sciences et Technologies, Lille, France, 2014.

[37] Toubin, H., Bailly, D., and Costes, M., "Improved Unsteady Far-Field Drag Breakdown Method and Application to Complex Cases," *AIAA Journal*, Vol. 54, No. 6, 2016, pp. 1907–1921.